




Article

Synthesis and Characterization of $\text{LaNi}_{0.5}\text{Ti}_{0.5}\text{O}_3$ and $\text{La}_2\text{NiTiO}_6$ Double Perovskite Nanoparticles

José Córdova-Calderón ¹, Pablo V. Tuza ^{1,*} and Mariana M. V. M. Souza ²

¹ Departamento de Energía y Mecánica, Carrera de Petroquímica, Universidad de las Fuerzas Armadas—ESPE, Sangolquí EC170501, Ecuador; jacordova8@espe.edu.ec

² Escola de Química, Universidade Federal do Rio de Janeiro (UFRJ), Centro de Tecnologia, Bloco E, Sala 206, CEP, Rio de Janeiro 21941-909, RJ, Brazil; mmattos@eq.ufrj.br

* Correspondence: pvtuza@espe.edu.ec; Tel.: +593-32810206 (ext. 4303)

Abstract: In the present work, $\text{LaNi}_{0.5}\text{Ti}_{0.5}\text{O}_3$ and $\text{La}_2\text{NiTiO}_6$ nanoparticles were synthesized by the modified Pechini method. $\text{LaNi}_{0.5}\text{Ti}_{0.5}\text{O}_3$ was calcined at 1073 K for 17 h or 100 h, while $\text{La}_2\text{NiTiO}_6$ was calcined at 1273 K for 135 h. The double perovskite calcined at 1073 K for 17 h presented orthorhombic symmetry with $Pbnm$ space group, mean particle size was 31.9 ± 1 nm, random ordering of Ni^{2+} and Ti^{4+} cations, Néel temperature close to 15 K, and magnetic moment of $1.29 \mu_B$. By increasing the calcination time, this material showed the same symmetry and space group, a mean particle size of 50.7 ± 2 nm, short-range ordering of Ni^{2+} and Ti^{4+} cations, Néel temperature around 12 K, and magnetic moment of $0.96 \mu_B$. $\text{La}_2\text{NiTiO}_6$ presented a monoclinic crystal structure, with $P2_1/n$ space group, mean particle size of 80.0 ± 5 nm, rock salt ordering of Ni^{2+} and Ti^{4+} , Néel temperature of approximately 23 K, and magnetic moment of $2.75 \mu_B$.

Keywords: double perovskite; $\text{LaNi}_{0.5}\text{Ti}_{0.5}\text{O}_3$; $\text{La}_2\text{NiTiO}_6$; nanoparticles



Citation: Córdova-Calderón, J.; Tuza, P.V.; Souza, M.M.V.M. Synthesis and Characterization of $\text{LaNi}_{0.5}\text{Ti}_{0.5}\text{O}_3$ and $\text{La}_2\text{NiTiO}_6$ Double Perovskite Nanoparticles. *Materials* **2022**, *15*, 2411. <https://doi.org/10.3390/ma15072411>

Academic Editor: Arunas Ramanavicius

Received: 23 February 2022

Accepted: 23 March 2022

Published: 25 March 2022

Publisher's Note: MDPI stays neutral with regard to jurisdictional claims in published maps and institutional affiliations.



Copyright: © 2022 by the authors. Licensee MDPI, Basel, Switzerland. This article is an open access article distributed under the terms and conditions of the Creative Commons Attribution (CC BY) license (<https://creativecommons.org/licenses/by/4.0/>).

1. Introduction

Perovskites are materials represented by the formula ABX_3 . A cation can be an alkali, alkali earth, or lanthanide metal, B cations are transition metals, and X can be oxygen or a halide [1]. The structure can be illustrated by octahedra layers, formed by octahedra sharing vertices, in which X atoms are found. The B cations occupy 6-octahedrally coordinated sites in the octahedra center, while A cations are located in dodecahedral coordinated sites. These A cations are placed in the cavities between octahedra. Double perovskites are mixed oxides, which can be formed when B cations are replaced by B' cations, including the equimolar substitution. There are three B-cation sublattice types known for double perovskites: random, rock salt, and layered [2]. The rock salt and layered double perovskites show ordered arrangement.

The multiple properties observed in perovskites make these materials attractive for electrochemical [3], electronic [4], spintronic [5], and catalytic applications. For example, the reforming of methane, which includes partial oxidation, steam reforming, and CO_2 reforming, has been carried out using catalysts derived from perovskites [6]. The reforming of methane is employed to produce H_2 , which can be used for naphtha reforming and ammonia production.

Nanoparticles can be used as nanocatalyst precursors for hydrogen production [7]. Nanocatalysts would decrease the cost of Fischer–Tropsch synthesis or enable competitive biofuel production compared to crude oil [8].

Nanoparticles of La, Ti, and Ni-based perovskite were used as catalysts for the steam reforming of methane [9,10]. These materials present random [11] or rock salt [12–14] B and B' cation ordering.

La, Ni, and Ti-containing perovskites have been prepared by various synthesis methods. Rodríguez et al. [11] synthesized the $\text{LaNi}_{1-x}\text{Ti}_x\text{O}_3$ ($0 \leq x \leq 0.5$) system using the

liquid mix technique, with synthesis temperature ranging from 723 to 1073 K, for several days. This same group synthesized La_2MTiO_6 ($M = \text{Ni}, \text{Co}$) compounds, using the aforementioned preparation method, and final thermal treatment in the range of 723 to 1173 K [12]. In these last two cases, the particle size was not reported. Yang et al. [15] synthesized the $\text{LaNi}_{1-x}\text{Ti}_x\text{O}_3$ perovskites using the amorphous citrate decomposition method, with final heat treatment ranging between 973 to 1273 K, for 10 h. In this last case, $\text{LaNi}_{0.5}\text{Ti}_{0.5}\text{O}_3$ was used as an acetone sensor. Pérez-Flores et al. [13,16] synthesized $\text{La}_{2-x}\text{Sr}_x\text{NiTiO}_{6-\delta}$ ($0 \leq x \leq 0.5$) materials using a final temperature treatment of 1773 K, for 24 h, with an average crystallite size of approximately 8 nm. Moreover, this same group reported the synthesis of the $\text{La}_{2-x}\text{NiTiO}_6$ ($0 \leq x < 0.2$) perovskites [17], along with $\text{La}_2\text{NiTiO}_6$ [18]. For the last double perovskite, the particle size ranged from 40 to 80 nm. Yang et al. [14] synthesized $\text{La}_2\text{Ni}(\text{Mn}_{1-x}\text{Ti}_x)\text{O}_6$ materials using the solid-state reaction, employing a final thermal treatment at 1773 K, for 3 h. $\text{LaNi}_{0.5}\text{Ti}_{0.5}\text{O}_3$, $\text{LaNi}_{0.5}\text{Ti}_{0.45}\text{Co}_{0.05}\text{O}_3$, and $\text{LaNi}_{0.45}\text{Co}_{0.05}\text{Ti}_{0.5}\text{O}_3$ synthesized by the modified Pechini method, coupled to a final heat treatment of 1073 K, for 17 h, with crystallite sizes of 27.1 nm, 35.8 nm, and 32.7 nm, respectively, were reported in previous works [9,10,19].

Furthermore, no works of $\text{LaNi}_{0.5}\text{Ti}_{0.5}\text{O}_3$ and $\text{La}_2\text{NiTiO}_6$ double perovskite nanoparticles were reported in the literature, using thermal treatments with final temperatures lower than those used in our work.

This article aims to study the structural and magnetic properties of $\text{LaNi}_{0.5}\text{Ti}_{0.5}\text{O}_3$ and $\text{La}_2\text{NiTiO}_6$ double perovskite nanoparticles, synthesized with a calcination temperature lower than the corresponding thermal conditions reported for the same double perovskites.

2. Materials and Methods

2.1. Synthesis

Nanoparticles of La, Ni, and Ti-containing double perovskites were prepared by the modified Pechini method [20]. Metal to the citric acid molar ratio of 1:2 and citric acid to ethylene glycol molar ratio of 1:4 were used for the synthesis. Adequate amounts of precursors (lanthanum nitrate hexahydrate ($\text{La}(\text{NiO}_3)_3 \cdot 6\text{H}_2\text{O}$, 99.5%), nickel nitrate hexahydrate ($\text{Ni}(\text{NiO}_3)_2 \cdot 6\text{H}_2\text{O}$, 97%), and titanium isopropoxide ($\text{C}_{12}\text{H}_{28}\text{O}_4\text{Ti}$, 97%) from Sigma-Aldrich) were dissolved in water. For the case of titanium, it was dissolved in 30 mL of nitric acid solution (3.4 mol L^{-1}) after isopropoxide evaporation. Initially, titanium citrate was prepared by heating titanium solution to 333 K for citric acid addition. Next, ammonium hydroxide was added to the titanium citrate solution in a volume close to nitric acid. Then, this last solution was aged overnight at room temperature. Lanthanum and nickel citrates were prepared using the methodology of titanium citrate preparation, except the ammonium hydroxide addition. Citrates were mixed at room temperature and heated up to 363 K with the addition of ethylene glycol to form a polyester solution. This final solution was aged similarly to metal citrate solution, with subsequent evaporation at 333 K, calcined at 513 K for 1 h, and 723 K for 4 h, using a heating rate of 2 K min^{-1} , milled in an agate mortar, obtaining the precursor.

Sample 1 was obtained by precursor calcination in air at 1073 K for 17 h. Sample 2 was synthesized by subsequent milling in agate mortar and calcination of Sample 1 at 1073 K for 100 h. Finally, Sample 3 was prepared by calcination of the precursor in air at 1173 K for 17 h, milled in an agate mortar, and calcined again at 1273 K for 135 h.

2.2. Characterization

The chemical composition of the samples was determined by X-ray fluorescence (XRF) using a Rigaku Primini spectrometer equipped with a Pd X-ray tube operating at 50 W (40 kV, 1.25 mA) and a ZSX software package. A 200 mg sample mass was placed in a polyethylene sample cup, covered with a thin polypropylene film, and then fixed with a ring.

X-ray diffraction (XRD) measurements were performed in a Rigaku Miniflex II X-ray diffractometer equipped with a graphite monochromator, using $\text{CuK}\alpha$ radiation (30 kV and

15 mA). XRD patterns of as-prepared samples were recorded over the 2θ range of $5\text{--}90^\circ$, step size and counting time per step equal to 0.02° and 6 s. A quartz sample holder was employed, on which a sample layer close to 300 mg was placed.

Rietveld method of X-ray diffraction patterns was performed using Fullprof Suite Program 3.0 [21]. The structure models of $\text{LaNi}_{0.5}\text{Ti}_{0.5}\text{O}_3$ (ICSD: 88851, [22]) and $\text{La}_2\text{NiTiO}_6$ (ICSD: 95977, [22]) double perovskites were employed for structure refinement of calcined materials at 1073 K (Sample 1 and Sample 2), and 1273 K (Sample 3), respectively. The background was defined with a 4th-order polynomial and refined simultaneously with the scale factor, unit cell parameters, peak shape parameters of the pseudo-Voigt function, atomic coordinates, together with the sample displacement, Sycos. For convergence achievement, xO2 from Sample 1 and zO1, and zO3 from Sample 3 were not refined. Sycos is the ratio between a parameter accounting for the sample displacement error, in degrees, and cosine of θ angle, where θ is measured in radians [23]. The isotropic displacement parameter was maintained at the value equal to 0.5 \AA^2 , as suggested for atoms in a metal oxide [24]. The fraction of site occupancy was not refined and was maintained at the value reported by ICSD [22] (see columns five and six from Table S1), except that of Ni^{2+} and Ti^{4+} from Sample 3.

Crystallite size was determined by the Scherrer equation. This equation was applied to (112) peak for Sample 1 and Sample 2, or $(\bar{1}12)$ peak for Sample 3, found at 2θ equal to 32.18° .

Micrographs were obtained from a scanning electron microscope (SEM, Model Quanta™ 450 FEG, FEI Company, Hillsboro, OR, USA) operating with an accelerating voltage of 20 kV. Before the analysis, the samples were coated by sputtering with an Au-containing film. Micrographs were analyzed with ImageJ version 1.52 v program [25]. Mean particle size was obtained using 100 particles.

DC magnetic measurements as a function of temperature, in the zero-field-cooled process, applying a magnetic field of 100 Oe, were performed using an MPMS 3 SQUID magnetometer in the temperature range 2–250 K (Sample 1), and Cryogenic SX-600 SQUID magnetometer in the temperature range 2–120 K (Sample 2 and Sample 3).

3. Results and Discussions

Table S1 shows the chemical composition of the samples determined by XRF. Compared to the corresponding theoretical counterparts, these values present minor variations. These differences can be attributed to equipment measurement errors and confirm the accuracy of the preparation method.

Figure 1 depicts the observed, calculated, and difference XRD patterns of the as-prepared double perovskites. For the case of Sample 1 and Sample 2, a single phase was obtained without any impurity. Sample 3 was composed of $\text{La}_2\text{NiTiO}_6$ and TiO_2 , with phase percentages equal to 97.28 % and 2.72 %, respectively. These values can be verified in Figure S1 and Table S2 of the Supplementary Material. Thus, Sample 3 was almost a single phase. The structural parameters and R-factor values are reported in Table S1, while the bond distance and bond angles are reported in Table S3. The unit cell parameters, atomic coordinates, the fraction of site occupancy values (Sample 3) and bond distance, along bond angles from the as-prepared double perovskites, are close to the values reported by ICSD [22].

Moreover, R-factor values from the Rietveld refinement are expected for the assumed experimental conditions. Thus, Sample 1 and Sample 2 have orthorhombic symmetry with the $Pbnm$ space group. Further, Supplementary Material Figure S2 presents the Rietveld refinement of Sample 3, using $Pbnm$ space group (ICSD: 88851, [22]). Furthermore, Table S4 shows the respective Rietveld refinement results. The Bragg factor from this Table is higher than that obtained from the $P2_1/n$ space group (3.89 (Table S4) vs. 3.14 (Table S1)). The same tendency was observed for the case of the chi-square value (1.82 (Table S4) vs. 1.64 (Table S1)). Therefore, Sample 3 shows monoclinic symmetry, with $P2_1/n$ space group. The symmetry and space group are according to that reported in

the literature for the $\text{LaNi}_{0.5}\text{Ti}_{0.5}\text{O}_3$ [11] (Sample 1 and Sample 2) and $\text{La}_2\text{NiTiO}_6$ [12–14] (Sample 3). The Glazer notation for as-synthesized materials is $a^-a^-c^+$, as reported for the case of the orthorhombic [19] and monoclinic [26] symmetries. Verification of the crystal structure was performed from the indexation of each XRD pattern, using McMaille software [27], with calculations reported in Figures S3–S8 of the Supplementary Material. Each double perovskite crystal structure is indicated in Figure 1, which was drawn using VESTA software [28].

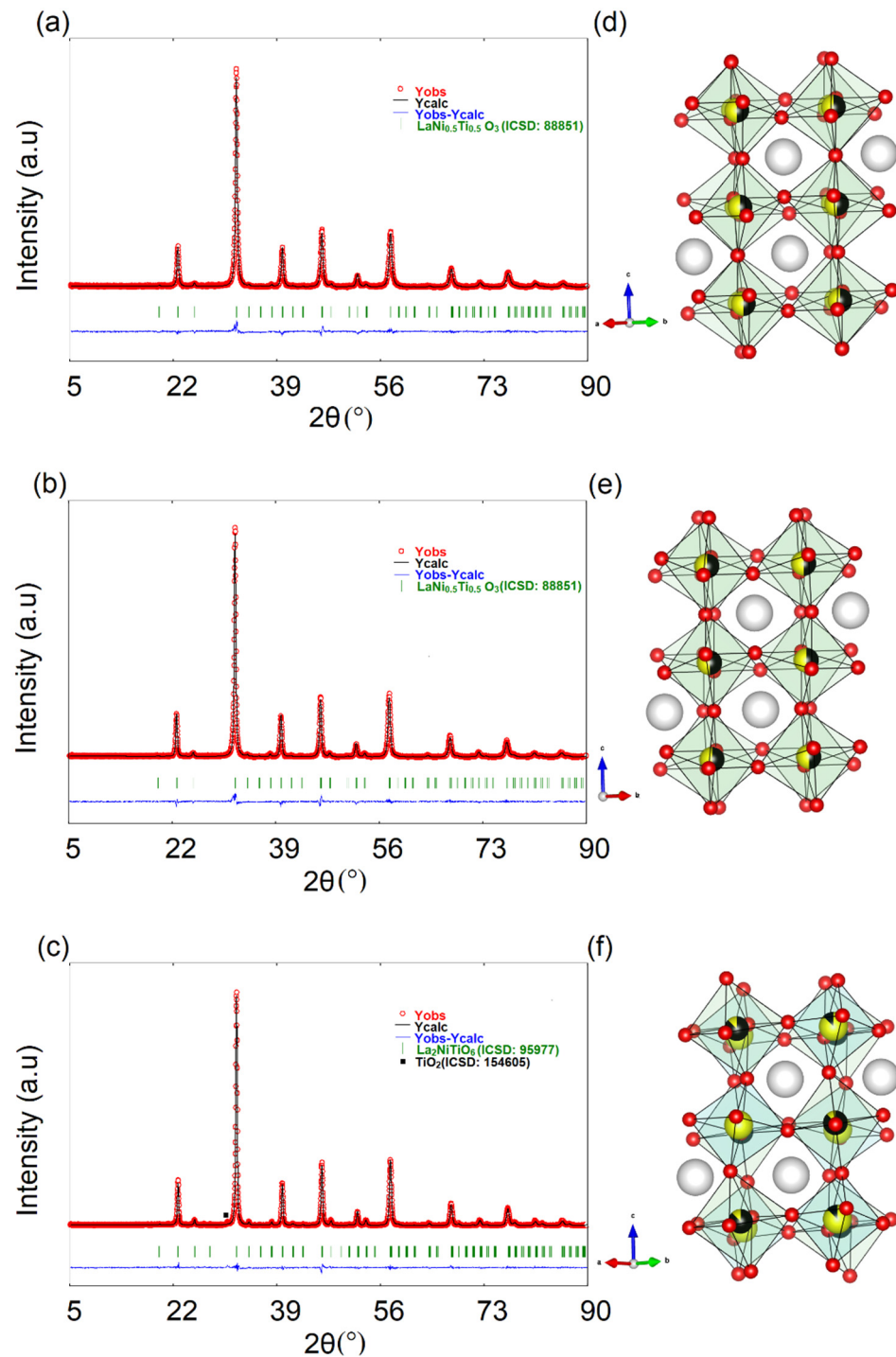


Figure 1. Observed (red symbols), calculated (black line) and difference (blue line) X-ray diffraction profiles of (a) Sample 1, (b) Sample 2 and (c) Sample 3. Crystal structure of (d) Sample 1, (e) Sample 2, and (f) Sample 3. (White, black, yellow, and red spheres denote La, Ni, Ti, and O atoms, respectively).

FEG-SEM images of the as-synthesized materials are shown in Figure 2. Sample 1 and Sample 2 materials are composed of agglomerated nanoparticles (Figure 2a,b). Aggregated particles at the nanoscale form Sample 3 are shown in Figure 2c. The mean particle sizes of Sample 1, Sample 2, and Sample 3 were equal to 31.9 ± 1 nm, 50.7 ± 2 nm, and 80.0 ± 5 nm, respectively. The measured particle sizes are in accordance with the respective crystallite sizes (Sample 1: 27.1 nm; Sample 2: 32.4 nm; Sample 3: 39.8 nm; Table S1).

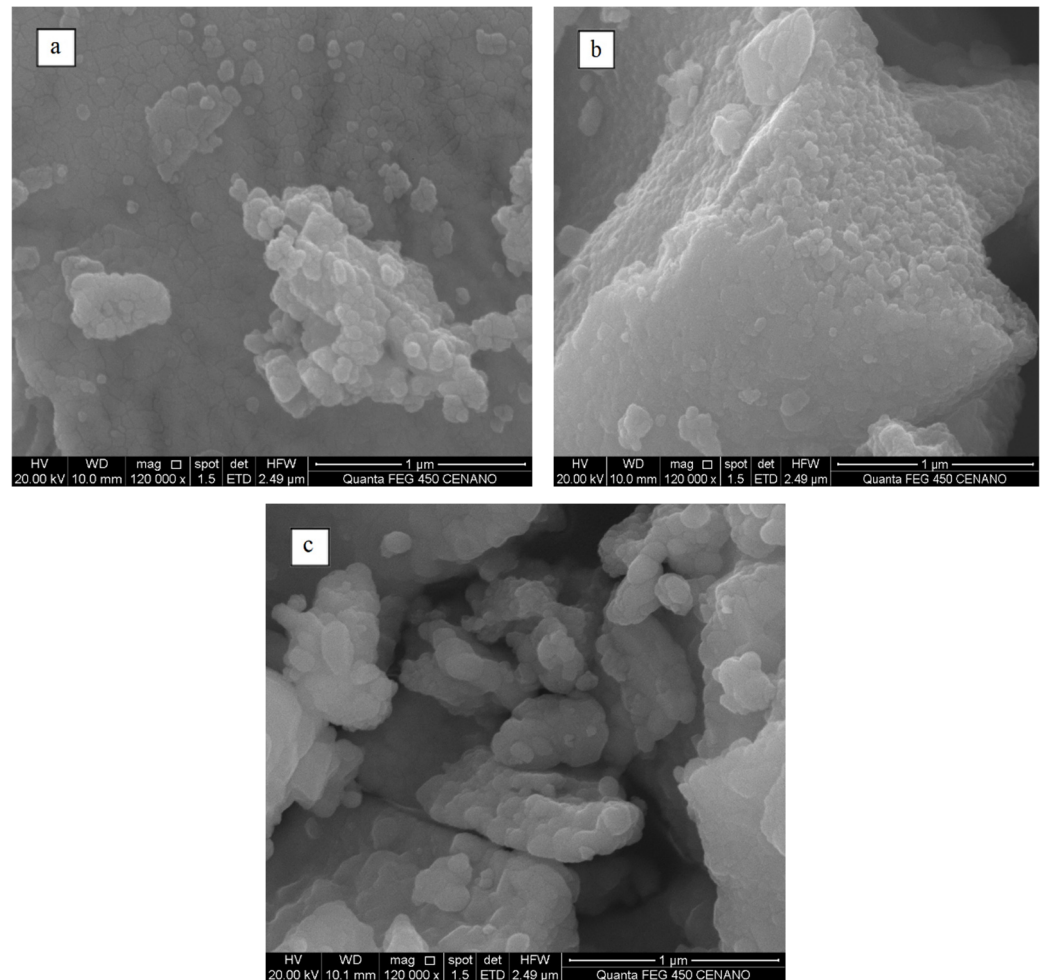


Figure 2. FEG-SEM images of (a) Sample 1, (b) Sample 2, and (c) Sample 3.

Figure 3 shows the magnetization and the respective inverse as a function of temperature, under zero-field cooling conditions.

$\chi_m T$ vs. T for Sample 1 is depicted in Supplementary Material Figure S9. Sample 1 shows Néel temperature around 15 K, as evidenced in Figure S9. This is the temperature at which a steep decrease in $\chi_m T$ values occurs, as the sample is cooled during the analysis [29]. The evolution of $\chi_m T$ with temperature is in agreement with that reported for the $\text{LaNi}_{0.5}\text{Ti}_{0.5}\text{O}_3$ [11]. Sample 2 and Sample 3 present Néel temperature around 12 K and 23 K, respectively. This last value is close to the respective values found in the work of Pérez-Flores et al. [13] and Rodríguez et al. [12] (25 K), or presented by Yang et al. [14] (17 K).

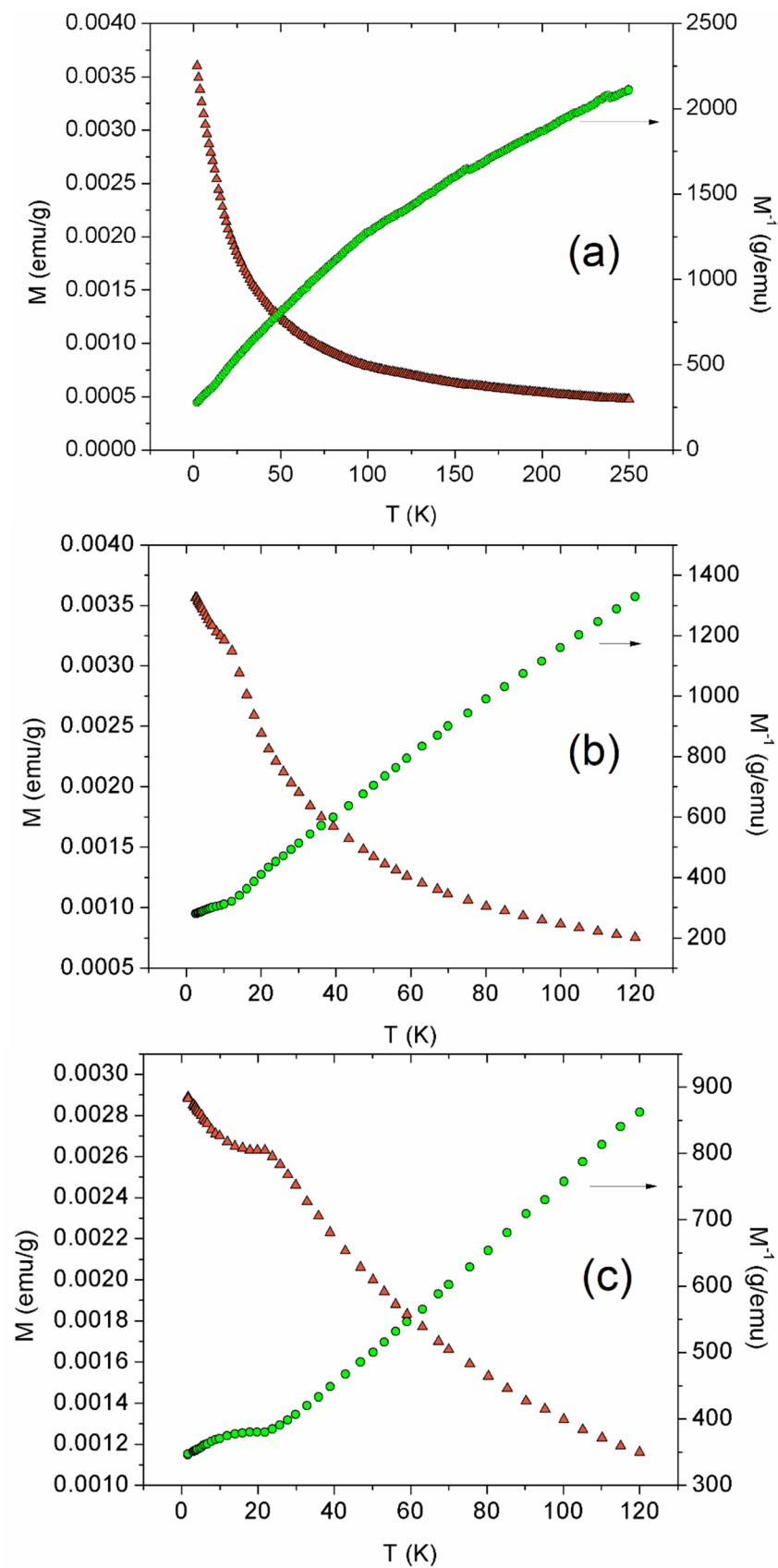


Figure 3. Variation of M along with M^{-1} vs. temperature for (a) Sample 1, (b) Sample 2, and (c) Sample 3.

B and B' cation ordering increases with Néel temperature, up to 25 K in the χ_m vs. T curve, as reported for the $\text{La}_{2-x}\text{Sr}_x\text{NiTiO}_{6-\delta}$ system [13]. Since Sample 1 did not show any peak in the M vs. T curve (Figure 3), a random arrangement of B and B' cations is confirmed for this sample. The Néel temperature value for Sample 2 can be attributed to short-range ordering. B and B' short-range cation ordering was shown by Pérez-Flores et al. [13] for the case of the $\text{La}_{1.85}\text{Sr}_{0.15}\text{NiTiO}_6$ material, when compared to that observed for $\text{La}_2\text{NiTiO}_6$. Moreover, the rock salt ordering arrangement of B and B' cations can be assigned to Sample 3.

For the case of Sample 1 and Sample 3, B and B' cation ordering relates to symmetry determined from X-ray diffraction, coupled to the Rietveld method. The Néel temperature value for Sample 3 is indicative of B and B' cation ordering, with $P2_1/n$ space group [12–14]. On the other hand, the short-range order of Sample 2 fits adequately into the orthorhombic symmetry, as presented by Pérez-Flores et al. [13] for $\text{La}_{1.85}\text{Sr}_{0.15}\text{NiTiO}_6$ perovskite.

The inverse values of the magnetic susceptibility were fitted using the Curie–Weiss law for the effective magnetic moment calculation. Curie constant, Weiss temperature, and the range used for the fitting are presented in Table 1. The magnetic moment for Sample 1 and Sample 2 ($1.29 \mu_B$, and $0.96 \mu_B$, Table 1) are similar to the value found by Rodríguez et al. [11] ($0.93 \mu_B$) for the $\text{LaNi}_{0.5}\text{Ti}_{0.5}\text{O}_3$. It is essential to point out that this analysis was redone for Sample 2, using Physical Property Measurement System (Quantum Design) equipment, in the range 2–40 K, along with a magnetic field equal to 1000 Oe, and presented in Figure S10 of the Supplementary Material.

Table 1. Weiss temperature (θ), Curie constant (C), and the effective magnetic moments (μ_{eff}) for Sample 1, Sample 2, and Sample 3.

| Sample | ΔT (K) ^a | θ | C (emu K Oe ⁻¹ mol ⁻¹) | μ_{eff} (μ_B) |
|--------|-----------------------------|----------|-----------------------------------------------|-------------------------|
| 1 | 14–40 | –15 | 0.207456 | 1.29 |
| 2 | 14–40 | –12 | 0.114417 | 0.96 |
| 3 | 33–120 | –23 | 0.944706 | 2.75 |

^a Temperature range used for estimation of μ_{eff}

Moreover, the effective magnetic moment for Sample 3 ($2.75 \mu_B$, Table 1) is in agreement with the values reported for $\text{La}_2\text{NiTiO}_6$ ($3.12 \mu_B$, [12]; $3.09(2) \mu_B$, [13]).

4. Conclusions

Nanoparticles of $\text{LaNi}_{0.5}\text{Ti}_{0.5}\text{O}_3$ and $\text{La}_2\text{NiTiO}_6$ were synthesized using the modified Pechini method. $\text{LaNi}_{0.5}\text{Ti}_{0.5}\text{O}_3$ calcined at 1073 K for 17 h, showing orthorhombic symmetry with $Pbnm$ space group, with mean particle size equal to 31.9 ± 1 nm, Néel temperature value around 15 K, and magnetic moment of $1.29 \mu_B$. By changing 17 h to 100 h for the calcination time, this material presented the same crystal structure and space group, mean particle size equal to 50.7 ± 2 nm, Néel temperature value approximately 12 K, and magnetic moment of $0.96 \mu_B$. On the other hand, $\text{La}_2\text{NiTiO}_6$ showed a monoclinic crystal structure, with $P2_1/n$ space group, mean particle size equal to 80.0 ± 5 nm, Néel temperature value around 23 K, and magnetic moment of $2.75 \mu_B$. The Glazer notation $a^-a^+c^+$ can represent these as-synthesized perovskites.

Random Ni^{2+} and Ti^{4+} cation ordering was verified for the $\text{LaNi}_{0.5}\text{Ti}_{0.5}\text{O}_3$ sample synthesized with the shortest calcination time. Short-range ordering arrangement of these transition metals was assigned to $\text{LaNi}_{0.5}\text{Ti}_{0.5}\text{O}_3$, calcined for 100 h. In addition, the rock salt order of the Ni^{2+} and Ti^{4+} cations was confirmed for the $\text{La}_2\text{NiTiO}_6$.

Supplementary Materials: The following supporting information can be downloaded at: <https://www.mdpi.com/article/10.3390/ma15072411/s1>, Figure S1: Observed (red symbols), calculated (black line), and difference (blue line) XRD profiles of Sample 3, Figure S2: Observed (red symbols), calculated (black line) and difference (blue line) X-ray diffraction profile of Sample 3 using $Pbnm$ space group (ICSD: 88851, [1]), Figure S3: Both unit-cell parameters and corrected observed 2-theta

values based on the Rietveld Refinement of XRD data of Sample 1 to perform the indexation of the corresponding XRD pattern, Figure S4: Both unit-cell parameters and corrected observed 2-theta values based on the Rietveld Refinement of XRD data of Sample 2 to perform the indexation of the corresponding XRD pattern, Figure S5: Both unit-cell parameters and corrected observed 2-theta values based on the Rietveld Refinement of XRD data of Sample 3 to perform the indexation of the corresponding XRD pattern, Figure S6: Unit-cell parameters, the corrected observed and calculated peak positions, and the respective difference obtained from the McMaille software for the case of Sample 1, Figure S7: Unit-cell parameters, the corrected observed and calculated peak positions, and the respective difference obtained from the McMaille software for the case of Sample 2, Figure S8: Unit-cell parameters, the corrected observed and calculated peak positions, and the respective difference obtained from the McMaille software for the case of Sample 3, Figure S9: $\chi_m T$ vs. T curve showing the Néel temperature for Sample 1, Figure S10: Variation of M along with M^{-1} vs. temperature for Sample 2 from 2 to 40 K; Table S1: Structural parameters, average crystallite size, together with conventional discrepancy factors from Rietveld refinement of XRD data for Sample 1, Sample 2, and Sample 3 [30], Table S2: Structural parameters, results of phase analysis together with conventional discrepancy factors from Rietveld refinement of XRD pattern for Sample 3, Table S3: Bond distances and bond angles for Sample 1, Sample 2, and Sample 3, Table S4: Structural parameters, average crystallite size, together with conventional discrepancy factors from Rietveld refinement of XRD data for Sample 3.

Author Contributions: Conceptualization, J.C.-C., P.V.T. and M.M.V.M.S.; methodology, J.C.-C., P.V.T. and M.M.V.M.S.; software, J.C.-C., P.V.T. and M.M.V.M.S.; validation, J.C.-C., P.V.T. and M.M.V.M.S.; formal analysis, J.C.-C., P.V.T. and M.M.V.M.S.; investigation, J.C.-C., P.V.T. and M.M.V.M.S.; resources, J.C.-C., P.V.T. and M.M.V.M.S.; data curation, J.C.-C., P.V.T. and M.M.V.M.S.; writing—original draft preparation, J.C.-C., P.V.T. and M.M.V.M.S.; writing—review and editing, J.C.-C., P.V.T. and M.M.V.M.S.; visualization, J.C.-C., P.V.T. and M.M.V.M.S.; supervision, P.V.T. and M.M.V.M.S.; project administration, P.V.T. and M.M.V.M.S.; funding acquisition, P.V.T. All authors have read and agreed to the published version of the manuscript.

Funding: This research received no external funding.

Institutional Review Board Statement: Not applicable.

Informed Consent Statement: Not applicable.

Data Availability Statement: Not applicable.

Acknowledgments: The authors thank Carlos André de Castro Perez from Instituto Federal de Ciência e Tecnologia do Rio de Janeiro—IFRJ, Brazil—for Rietveld analysis. They are grateful to Professor Alexandre Novak from Laboratory of Low Temperatures at Physics Institute/UFRJ, Jilder Peña Serna, and Geraldo Cernicchiaro from the Brazilian Center for Research in Physics for the magnetic measurements and data treatment. They are also grateful to Andréa Maria Duarte de Farias and Francisco Luiz Correa Rangel from Nanotechnology Characterization Center (CENANO)/National Institute of Technology, Brazil, for FEG-SEM micrographs.

Conflicts of Interest: The authors declare no conflict of interest.

References

1. Subramani, T.; Voskanyan, A.; Jayanthi, K.; Abramchuk, M.; Navrotsky, A. A Comparison of Order–Disorder in Several Families of Cubic Oxides. In *Ordered and Disordered Cubic Systems: Pyrochlore to Fluorite, Now and the Horizon*; Thorogood, G.J., Finkeldei, S.C., Lang, M.K., Simeone, D., Eds.; Frontiers Media: Lausanne, Switzerland, 2022; pp. 34–54.
2. Anderson, M.T.; Greenwood, K.B.; Taylor, G.A.; Poeppelmeier, K.R. B-cation arrangements in double perovskites. *Prog. Solid State Chem.* **1993**, *22*, 197–233. [[CrossRef](#)]
3. Zhang, Y.; Tao, Y.; Yu, Z.; Lu, J.; Lim, S.Y.; Shao, J. Structure and electrochemical properties of titanate perovskite with in situ exsolution as a ceramic electrode material. *J. Electroceram.* **2020**, *45*, 29–38. [[CrossRef](#)]
4. George, G.; Ede, S.R.; Luo, Z. *Fundamentals of Perovskite Oxides: Synthesis, Structure, Properties and Applications*, 1st ed.; CRC Press: Boca Raton, FL, USA, 2020; pp. 185–226.
5. Kalanda, M.A.; Lobanovsky, L.S.; Gurskii, L.I.; Telesh, E.V.; Kotov, D.A.; Saad, A.; Adolphi, B.; Plötner, M. Structure and magnetic properties of $\text{Sr}_2\text{FeMoO}_{6\pm\delta}$. In *Physics, Chemistry and Application of Nanostructures*; Borisenko, V.E., Gaponenko, S.V., Gurin, V.S., Eds.; World Scientific: Hackensack, NJ, USA, 2009; pp. 248–251.

6. Bian, Z.; Wang, Z.; Jiang, B.; Hongmanorom, P.; Zhong, W.; Kawi, S. A review on perovskite catalysts for reforming of methane to hydrogen production. *Renew. Sustain. Energy Rev.* **2020**, *134*, 110291. [[CrossRef](#)]
7. Souza, M.M.V.M.; Aranda, D.A.G.; Schmal, M. Reforming of methane with carbon dioxide over Pt/ZrO₂/Al₂O₃. *J. Catal.* **2001**, *204*, 498–511. [[CrossRef](#)]
8. Budarin, V.; Shuttleworth, P.S.; Lanigan, B.; Clark, J.H. Nanocatalysts for Biofuels. In *Nanocatalysis Synthesis Applications*; Polshettiwar, V., Asefa, T., Eds.; John Wiley & Sons, Inc.: Hoboken, NJ, USA, 2013; pp. 595–614.
9. Tuza, P.V.; Souza, M.M.V.M. Steam Reforming of Methane Over Catalyst Derived from Ordered Double Perovskite: Effect of Crystalline Phase Transformation. *Catal. Lett.* **2016**, *146*, 47–53. [[CrossRef](#)]
10. Tuza, P.V.; Souza, M.M.V.M. B-cation partial substitution of double perovskite La₂NiTiO₆ by Co²⁺: Effect on crystal structure, reduction behavior and catalytic activity. *Catal. Commun.* **2017**, *97*, 93–97. [[CrossRef](#)]
11. Rodríguez, E.; Álvarez, I.; López, M.L.; Veiga, M.L.; Pico, C. Structural, Electronic, and Magnetic Characterization of the Perovskite LaNi_{1-x}Ti_xO₃ (0 ≤ x ≤ 1/2). *J. Solid State Chem.* **1999**, *148*, 479–486. [[CrossRef](#)]
12. Rodríguez, E.; López, M.L.; Campo, J.; Veiga, M.L.; Pico, C. Crystal and magnetic structure of the perovskites La₂MTiO₆ (M = Co, Ni). *J. Mater. Chem.* **2002**, *12*, 798–2802. [[CrossRef](#)]
13. Pérez-Flores, J.C.; Ritter, C.; Pérez-Coll, D.; Mather, G.C.; García-Alvarado, F.; Amador, U. Synthesis, structures and electrical transport properties of the La_{2-x}Sr_xNiTiO_{6-δ} (0 ≤ x ≤ 0.5) perovskite series. *J. Mater. Chem.* **2011**, *21*, 13195–13204. [[CrossRef](#)]
14. Yang, W.Z.; Liu, W.Z.; Lin, Y.Q.; Chen, X.M. Structure, magnetic, and dielectric properties of La₂Ni(Mn_{1-x}Ti_x)O₆ ceramics. *J. Appl. Phys.* **2012**, *111*, 084106. [[CrossRef](#)]
15. Yang, M.; Huo, L.; Zhao, H.; Gao, S.; Rong, Z. Electrical properties and acetone-sensing characteristics of LaNi_{1-x}Ti_xO₃ perovskite system prepared by amorphous citrate decomposition. *Sens. Actuators B Chem.* **2009**, *143*, 111–118. [[CrossRef](#)]
16. Pérez-Flores, J.C.; Ritter, C.; Pérez-Coll, D.; Mather, G.C.; Canales-Vázquez, J.; Gálvez-Sánchez, M.; García-Alvarado, F.; Amador, U. Structural and electrochemical characterization of La_{2-x}Sr_xNiTiO_{6-δ}. *Int. J. Hydrogen Energy* **2012**, *37*, 7242–7251. [[CrossRef](#)]
17. Pérez-Flores, J.C.; Pérez-Coll, D.; García-Martín, S.; Ritter, C.; Mather, G.C.; Canales-Vázquez, J.; Gálvez-Sánchez, M.; García-Alvarado, U.; Amador, U. A- and B-Site Ordering in the A-Cation-Deficient Perovskite Series La_{2-x}NiTiO_{6-δ} (0 ≤ x < 0.20) and Evaluation as Potential Cathodes for Solid Oxide Fuel Cells. *Chem. Mater.* **2013**, *25*, 2484–2494.
18. Pérez-Flores, J.C.; Castro-García, M.; Crespo-Muñoz, V.; Valera-Jiménez, J.F.; García-Alvarado, F.; Canales-Vásquez, J. Analysis of Performance Losses and Degradation Mechanism in Porous La_{2-x}NiTiO_{6-δ}: YSZ Electrodes. *Materials* **2021**, *14*, 2819. [[CrossRef](#)] [[PubMed](#)]
19. Souza, M.M.V.M.; Maza, A.; Tuza, P.V. X-ray powder diffraction data of LaNi_{0.5}Ti_{0.45}Co_{0.05}O₃, LaNi_{0.45}Co_{0.05}Ti_{0.5}O₃, and LaNi_{0.5}Ti_{0.5}O₃ perovskites. *Powder Diffr.* **2021**, *36*, 29–34. [[CrossRef](#)]
20. Vijatović, M.M.; Bobić, J.D.; Stojanović, B.D. History and challenges of barium titanate: Part I. *Sci. Sinter.* **2008**, *40*, 155–165. [[CrossRef](#)]
21. Rodríguez-Carvajal, J. Recent advances in magnetic structure determination by neutron powder diffraction. *Phys. B Condens. Matter* **1993**, *192*, 55–69. [[CrossRef](#)]
22. ICSD, Inorganic Crystal Structure Database. Available online: <https://bdec.dotlib.com.br/> (accessed on 1 December 2017).
23. Rodríguez-Carvajal, J. Fullprof Manual. Available online: <http://www.ill.eu/sites/fullprof/> (accessed on 1 December 2017).
24. Atfield, M.; Barnes, P.; Cockcroft, J.K.; Driessen, H. Advanced Certificate in Powder Diffraction (School of Crystallography, Birkbeck College, University of London). Available online: <http://pd.chem.ucl.ac.uk/pdnn/refine1/case.htm> (accessed on 1 October 2021).
25. Rasband, W.S. National Institutes of Health, Bethesda, Maryland, USA. Available online: <https://imagej.nih.gov/ij> (accessed on 1 October 2021).
26. Lidin, S. Quasicrystal Approximants. In *Handbook of Solid State Chemistry*; Dronskowski, R., Kikkawa, S., Stein, A., Eds.; Wiley-VCH: Weinheim, Germany, 2017; pp. 73–92.
27. Le Bail, A. Monte Carlo indexing with McMaille. *Powder Diffr.* **2004**, *19*, 249–254. [[CrossRef](#)]
28. Momma, K.; Izumi, F. VESTA 3 for three-dimensional visualization of crystal, volumetric and morphology data. *J. Appl. Crystallogr.* **2011**, *44*, 1272–1276. [[CrossRef](#)]
29. De Muro, I.G.; Insausti, M.; Lezama, L.; Pizarro, J.L.; Arriortua, M.I.; Rojo, T. Structural, Spectroscopic, Magnetic and Thermal Properties in the [SrM(C₃H₂O₄)₂(H₂O)₅].2H₂O (M = Mn, Fe, Co, Ni) System: Precursors of SrMO_{3-x} Mixed Oxides. *Eur. J. Inorg. Chem.* **1999**, *1999*, 935–943. [[CrossRef](#)]
30. Smith, G.S.; Snyder, R.L. FN: A Criterion for Rating Powder Diffraction Patterns and Evaluating the Reliability of Powder-Pattern Indexing. *J. Appl. Crystallogr.* **1979**, *12*, 60–65. [[CrossRef](#)]